ACS APPLIED MATERIALS & INTERFACES

Research Article

www.acsami.org

Biomimetic Magnetic Silk Scaffolds

Sangram K. Samal,[†,‡,§] Mamoni Dash,[∥] Tatiana Shelyakova,[⊥] Heidi A. Declercq,[#] Marc Uhlarz,[▽] Manuel Bañobre-López,[○] Peter Dubruel,[∥] Maria Cornelissen,[#] Thomas Herrmannsdörfer,[▽] Jose Rivas,[○,◆] Giuseppina Padeletti,[†] Stefaan De Smedt,[§] Kevin Braeckmans,[§] David L. Kaplan,*[,‡] and V. Alek Dediu*[,†]

[†]Consiglio Nazionale delle Ricerche−Institute for Nanostructured Materials, I-40129 Bologna-Roma, Italy

[‡]Department of Biomedical Engineering, Tufts University, 4 Colby Street, Medford, Massachusetts 02155, United States

[§]Laboratory of General Biochemistry and Physical Pharmacy, Ghent University, Ottergemsesteenweg 460, 9000 Ghent, Belgium

[∥]Polymer Chemistry & Biomaterials Research Group, Ghent University, Krijgslaan 281, S4-Bis, B-9000 Ghent, Belgium

[⊥]Laboratory of Biomechanics and Technology Innovation, NABI, Rizzoli Orthopaedic Institute, 40136 Bologna, Italy

[#]Department of Basic Medical Science − Tissue Engineering Group, Ghent University, De Pintelaan 185 (6B3), 9000 Ghent, Belgium

[▽]Dresden High Magnetic Field Laboratory (HLD-EMFL), Helmholtz-Zentrum Dresden-Rossendorf, Bautzner Landstrasse 400, 01328 Dresden, Germany

[○]International Iberian Nanotechnology Laboratory (INL), Av. Mestre José Veiga, 4715-330 Braga, Portugal

ABSTRACT: Magnetic silk fibroin protein (SFP) scaffolds integrating magnetic materials and featuring magnetic gradients were prepared for potential utility in magnetic-field assisted tissue engineering. Magnetic nanoparticles (MNPs) were introduced into SFP scaffolds via dip-coating methods, resulting in magnetic SFP scaffolds with different strengths of magnetization. Magnetic SFP scaffolds showed excellent hyperthermia properties achieving temperature increases up to 8 °C in about 100 s. The scaffolds were not toxic to osteogenic cells and improved cell adhesion and proliferation. These findings suggest that tailored magnetized silk-based biomaterials can be engineered with interesting features for biomaterials and tissue-engineering applications.

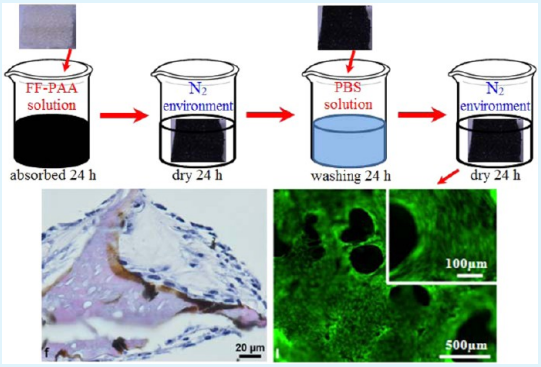

KEYWORDS: *magnetic nanoparticles, silk protein, magnetic scaffold, magnetic gradient, magnetic field, hyperthermia, biomaterials, tissue engineering*

1. INTRODUCTION

Polymeric biomaterials and their utilization as scaffolds in regenerative medicine have increased for various therapeutic needs. In particular, scaffolds for tissue engineering coupled to biomolecules and stem cells have accelerated the regeneration of tissue defects.[1−4] As a result, efforts have been dedicated to the development of manufacturing technologies for the production of customized scaffolds with reproducible internal morphology, leading to an increase in transport of biomolecules and thus improved tissue outcomes in vitro and in vivo.[5−11]

Silk fibroin protein has been investigated extensively and approved as a biomaterial by the U.S. Food and Drug Administration (FDA) for some biomedical applications.[12,13] As a natural biomaterial, silk has good mechanical properties, low inflammatory reactions, good permeability, and good blood compatibility. The properties of silk are derived from its chemistry and unique structure, which consists of hydrophobic β-sheet crystalline blocks staggered by hydrophilic amorphous acidic spacers.[14−16] Silk fibroin protein scaffolds consist of protein networks with physical cross-links preventing dissolution under physiological conditions. These silk scaffold networks are comprised of hydrophobic and hydrophilic moieties, with hydrophilic functional groups (−OH, −COOH, $-NH_2$, $-CONH_2$) able to chelate metal ions.[17−20] Furthermore, scaffold networks can be modified with new functional groups to enhance metal chelating properties and versatility for therapeutic use.[21−23]

Recent advances in the development of magnetic nanoparticles (MNPs) in various diagnostic and therapeutic applications have exploited the unique properties of MNPs and the ability to manipulate them externally via magnetic fields. MNPs are metal nanoparticles and have been widely used in many biomedical applications due to their biocompatibility, low cost, and sensitivity to external stimuli using an applied magnetic field. MNPs including Feridex (SPIO, Feridex-USA, Endorem-Europe) and Combidex (USPIO,

Received: January 20, 2015
Accepted: March 3, 2015
Published: March 3, 2015

DOI: 10.1021/acsami.5b00529
ACS Appl. Mater. Interfaces 2015, 7, 6282−6292

Combidex-USA, Sinerem-Europe) have already been FDA-approved or are in late-phase clinical trials as MRI contrast agents for cells of the reticulo-endothelial system. The incorporation of MNPs in polymeric networks provides magnetic responsive properties. Recently, the concept of scaffolds with internal magnetic gradients has been introduced, which provides an elegant way to overcome some localization challenges.[24,25] Among various strategies to design magnetic scaffolds, the incorporation of MNPs into polymeric solutions followed by cross-linking, or infusion methods, is most widely used.[26,27] Alternatively, magnetic scaffolds can be prepared by "in situ" synthesis of MNPs in the scaffold through coprecipitation of Fe^{2+} and Fe^{3+} salts by treatment with alkali solutions.[28−30] The incorporation of MNPs nanoparticles is expected to improve the scaffolds' bioactivity.[31−35]

Under a magnetic field, these types of scaffolds induce physical changes such as elongation, contraction, or bending.[36−38] These magnetic-sensitive biomaterials are useful in comparison to other stimuli-responsive biomaterials because magnetic stimulation acts at a distance (noncontact force) that is noninvasive and convenient to adapt for therapeutic devices.[39−42] The magnetic properties of scaffolds can be utilized to construct biomaterials for site-specific and/or time-controlled delivery, magnetic resonance imaging contrast agents, sensors, and artificial muscles.[26,43−48] This approach also includes various separation membranes and hyperthermia treatments under external magnetic stimuli.[49−52]

In this Article, an infusion technique was adopted to design two different types of magnetized silk scaffolds. The characteristics of these magnetite nanocomposite scaffolds were evaluated by investigating magnetic properties and thermal response to a remotely applied external magnetic field. The magnetic scaffolds biocompatibility was evaluated by seeding osteogenic cells onto it and observing differentiation in vitro. The present work is aimed to design magnetic silk scaffold via a simple strategy and understand their cellular response in vitro, which could lead to efficient magnetic silk-based biomaterials for tissue engineering applications.

2. EXPERIMENTAL SECTION

2.1. Materials. Cocoons from the *Bombyx mori* silkworm were obtained from Tajima Shoji Co. (Yokohama, Japan). Sodium carbonate (Na_2CO_3) and lithium bromide (LiBr) were purchased as reagent grade from Sigma−Aldrich or Fluka (St. Louis, MO) and used without further purification. Dialysis cassettes (Slide-a-Lyzer MWCO 3.5K) were purchased from Pierce Biotechnology Inc. (Rockford, IL). Water dispersed magnetic nanoparticles 25 mg/mL Ferrofluids poly-DL-aspartic acid (FF-PAA) was purchased from Chemicell GmbH (Berlin, Germany), approximately ∼50−100 nm.

2.2. Preparation of Aqueous Silk Fibroin Protein Solution. Aqueous silk solutions were prepared on the basis of our published protocols.[53,54] Briefly, whole cocoons were cut into small pieces and were boiled in a 0.02 M aqueous solution of $NaCO_3$. The remaining fibroin was rinsed thoroughly in deionized water and allowed to dry overnight. The dry fibroin was then dissolved in a 9.3 M aqueous solution of LiBr at 60 °C for 6 h. The LiBr was removed from the solution over the course of 48 h by dialysis cassettes (Slide-a-Lyzer MWCO 3.5K, Pierce Biotechnology Inc., Rockford, IL), and remaining particulates were removed by centrifugation and syringe-based microfiltration (5 μm pore size, Millipore Inc., Bedford, MA). This process enables the production of 8−10 w/w % silk in water. Silk solutions with lower concentrations were prepared by diluting the above solution with double distilled deionized water. The final silk concentration of the solution was monitored by drying 1 mL of silk solution samples in a plastic Petri dish at 60 °C (American Scientific Products, constant temperature oven, model DK-42) and weighing the resulting dried films.

2.3. Silk Scaffold Fabrication. Salt leached porous silk scaffolds were prepared according to the procedure described in the literature.[55−58] Briefly, 4 g of the granular NaCl (particle size, 850−1000 μm) was added slowly to a cylindrically shaped container with 2 mL of silk solution. The container was covered to reduce the evaporation rate and kept at room temperature for homogeneous distribution of the solution. After 24 h, the container was uncovered and immersed in Milli-Q water with stirring for 24 h to leach out NaCl particles. The silk scaffolds of desired dimensions were punched-out with punch-pressure equipment.

2.4. Diffusion of MNPs into Silk Scaffolds. The diffusion experiments were performed by using disposable cuvettes (45 × 13 mm), both sides of the cuvette were closed, and the upper part of the cuvette was cut to place the scaffold. The silk scaffolds (d = 12 mm, h = 9 mm) were placed in the middle of the open cuvette and filled with PBS solution. The MNPs were injected from one end of the cuvette, and a static permanent magnet (d = 80 mm, h = 10 mm, B_r = 1.2 T) was placed on the opposite side at a distance of 10 cm from the cuvette. Evaluation of magnetic field and its gradient in the scaffold and MNPs regions was obtained using Comsol 3.5 software.

2.5. Magnetization of Silk Scaffold. The porous silk scaffolds were immersed in 5 mL of MNPs for 24 h to allow the filling of MNPs in the micronano pores of the scaffolds by capillary absorption. The functional groups such as acid (−COOH) and amino ($-NH_2$) groups of scaffolds chelate MNPs.[17] The MNP-absorbed silk scaffolds were then dried under nitrogen atmosphere at room temperature. To wash off excess MNPs, the magnetic scaffolds samples were immersed in simulated body fluids and agitated over a period of 24 h and dried under nitrogen atmosphere. The magnetic scaffolds with different magnetization values were generated by altering the concentrations of MNPs. The sample codes with respect to the MNPs concentration used for the magnetization are shown in Table 1.

Table 1. Sample Abbreviations with Respect to the Amount of MNPs Soaked into the Silk Scaffolds

sample	abbreviation	MNPs (μL/mL)
SFP scaffolds	SFPS	0
magnetic SFP scaffolds with low concentration MNPs	MSFPSa	50
magnetic SFP scaffolds with high concentration MNPs	MSFPSb	250

2.6. Magnetization Measurements. Magnetization measurements were performed using a Superconducting Quantum Interference Device (SQUID) magnetometer. This instrument measures the total magnetic moment of a sample, including all atomic and molecular magnetic contributions. The magnetization of the sample was calculated as the ratio between magnetic moment and sample mass. A microbalance (Sartorius model M3P) was used to determine sample masses. Each sample was fixed to a custom-made sample holder, which ensures a canceling of background contributions. The magnetic field was either swept at human-body temperature or held constant during a temperature sweep. Having reached predetermined values of field and temperature, the samples were consistently moved through a pick-up coil system connected to the SQUID via a flux transformer. The sample movement effects a magnetic flux change in the superconducting pick-up circuit, which is sensed and amplified by a SQUID sensor and its feedback control circuit. The SQUID output signal is directly proportional to the sample's magnetic moment. Knowing the sample geometries, the samples' demagnetization factors were calculated to determine the quantitatively correct internal magnetic field values. The results showed that the demagnetization contributions were well below 1% of the measured magnetizations and can thus be neglected. The magnetization of the pure, nonmagnetized silk protein scaffold was smaller than 0.1 emu/g at T = 310 K and at any magnetic field and, hence, may be neglected.

DOI: 10.1021/acsami.5b00529
ACS Appl. Mater. Interfaces 2015, 7, 6282−6292

2.7. Magnetic-Hyperthermia Measurement. Two hundred microliters was inserted in a Teflon crucible located in the midpoint of a water cooled copper coil, where the magnitude of the oscillating magnetic field generated by an AC current circulating through it is maximum. The experimental values of frequency and intensity of this alternating magnetic field used in the experiments were 293 kHz and 30 mT, respectively. An optical fiber immersed in the ferrofluid then measured the temperature increase as a function of the time. The main advantage of magnetic hyperthermia is that we can remotely control externally the activation of the nanoparticles embedded in the scaffold to behave as small nanoheaters, so increasing the local temperature and inducing growth factors release for tissue regeneration.

2.8. Scaffold Morphology by Field Emission Scanning Electron Microscopy (FE-SEM) and Composition by Energy Dispersive X-ray Spectrometry (EDS). FE-SEM and EDS analyses were performed on a high brilliance LEO 1530 apparatus equipped with an EDS INCA 450, a Schottky-type field emission electron source, and a four-sectors backscattered electron detector (BSE) (Leo Electron Microscopy Ltd., Zeiss SMT company, Oberkochen, Germany). Prior to analysis, all samples were fractured using tweezers followed by coating with a thin conductive layer. In the case of FE-SEM-EDS analysis, samples were coated with a thin layer of chromium to prevent the accumulation of electrostatic charge at the surface and to avoid the resulting effects by using a Bal-Tech SCD 500 equipped with turbo pumping for ultra clean preparations at a pressure of 5×10^{-3} mbar that deposits a chromium film with a constant thickness of about 0.5 nm. The high-resolution images were recorded both in the secondary electron image (SEI) and in the backscattered electron image (BSE) mode at different acceleration voltages ranging from 20 to 2 kV (low-voltage SEM) producing high primary electron brightness even at low accelerating potentials.

2.9. Thermogravimetric Analysis (TGA). TGA experiments were performed with a TA Instruments, Q500 thermo-balance (TA Instruments, Milan, Italy) with Thermogravimetric Analyzer software (Universal Analysis 2000). Sample weights were between 4 and 6 mg and were scanned at 10 °C min^{-1}. The temperature range was 30−700 °C under a 60 mL min^{-1} flow rate of nitrogen.[59]

2.10. Differential Scanning Calorimetry (DSC). Thermodynamic parameters DSC of the samples were assessed on a Mettler DSC822e module (Mettler Toledo, Milan, Italy) controlled by the STARe software under a nitrogen atmosphere at 80 mL min^{-1} flow rate with three scans. Samples of 3−5 mg were weighed in standard 40 μL aluminum pans, and an empty pan was used as reference. Measurements were performed in accordance with ASTM D3418 methods under a nitrogen flow rate of 80 mL min^{-1} according to the following protocols: (a) first heating scan from −20 to 150 °C at 10 °C min^{-1} and 3 min of isothermal conditions at the end; (b) first cooling scan from 150 to −20 °C at −10 °C min^{-1} and 3 min of isothermal conditions at the end; and (c) second heating scan from −20 to 320 °C at 10 °C min^{-1}.

2.11. Cell Culture. *2.11.1. Cell Culture and Cell Seeding on Magnetic Scaffolds.* MC3T3-E1 cells (mouse calvaria preosteoblast cells, subclone 14, ATCC) were cultured in α-MEM L-glutamax (Gibco Invitrogen) supplemented with 10% fetal bovine serum (FBS, Gibco Invitrogen) and 0.5 vol % penicillin-streptomycin (10 000 U/ml to 10 000 μg/mL, Gibco Invitrogen) (standard medium). Cells were cultured at 37 °C in a humidified atmosphere of 5% CO_2. The blank and magnetic silk scaffolds (d 6 mm, h 5 mm) were sterilized using ethylene oxide cold cycle (Maria Middelares, Ghent, Belgium). Before cell seeding, the scaffolds were immersed in serum-free α-MEM medium in 24-well plates. After 24 h, the scaffolds were placed into 24-well tissue culture dishes (for suspension culture). Cells were seeded at a density of 1×10^6 cells/40 μL/scaffold for cell viability/proliferation and colonization and were allowed to adhere for 4 h. Only for the Presto Blue assay were cells seeded at a density of 0.3×10^6 cells/40 μL/scaffold. Standard culture medium (160 μL) was added to each well, and the seeded scaffolds were further incubated overnight. After 24 h, cell/scaffold constructs were placed in 12-well plates. Osteogenic medium (3 mL), consisting of standard medium supplemented with 100 μM L-ascorbic acid 2-phosphate (Sigma-Aldrich), 10 nM dexamethasone (Sigma-Aldrich), and 10 mM β-glycerophosphate (Sigma-Aldrich), was added, and the cell/scaffold constructs were cultured for 21 days (5% CO_2/95% air, 37 °C).

2.11.2. Characterization of Cell/Scaffold Constructs. Cell adhesion, proliferation, and colonization were evaluated at different time points with the following analyses.

2.11.2.1. Fluorescence Microscopy. To visualize cell adhesion and colonization of the scaffolds, cell/scaffold constructs were evaluated using fluorescence microscopy after performing live/dead staining. After being rinsed with PBS, the supernatant was replaced by 1 mL of PBS solution supplemented with 2 μL (1 mg/mL) of calcein AM (Anaspec, USA) and 2 μL of propidium iodide (1 mg/mL) (Sigma-Aldrich). Cultures were incubated for 10 min at room temperature, washed twice with PBS solution, and evaluated by fluorescence microscopy (Olympus inverted Research System Microscope, type U-RFL-T, Cell software, Olympus, Belgium). Evaluations were done postseeding at day 1, 7, 14, and 21.

2.11.2.2. Prestoblue Viability. The Prestoblue assay (Invitrogen) was applied to quantify cell viability and proliferation in the cell/scaffold constructs. Prestoblue is a blue nonfluorescent, cell permeable compound (resazurin-based solution) that is reduced by living cells into a fluorescent compound (resorufin). PrestoBlue reagent (100 μL) was added to 900 μL of culture medium/scaffold and incubated for 2 h at 37 °C. The fluorescence intensity was performed on the Wallac 1420 Viktor 3TM plate reader (PerkinElmer, Inc.) at 535 nm excitation and 615 nm emission. Triplicate measurements were performed postseeding at day 1, 7, 14, and 21.

2.11.2.3. Histology. Cell/scaffold constructs were rinsed with PBS solution, fixed with 4% phosphate (10 mM) buffered formaldehyde (pH 6.9) (4 °C, 24 h), dehydrated in a graded alcohol series, and embedded in paraffin. The scaffolds were sectioned 5−7 μm and stained with hematoxylin and eosin (H&E) and mounted with mounting medium (cat. no. 4111E, Richard-Allan Scientific).

3. RESULTS AND DISCUSSION

3.1. Salt-Leached Silk Scaffold Fabrication. Scaffolds for tissue formation require suitable porosity to facilitate cell attachment, proliferation, migration, and nutrient and waste transport into and out of the scaffold system.[60,61] There are a number of fabrication methods that have been utilized to design porous silk-based scaffolds toward this goal, including freeze-drying, gas foaming, and salt porogen leaching.[16,62,63] The salt-leached silk scaffolds are generally stiffer and possess rough surfaces due to the partial solubilization of NaCl and β-

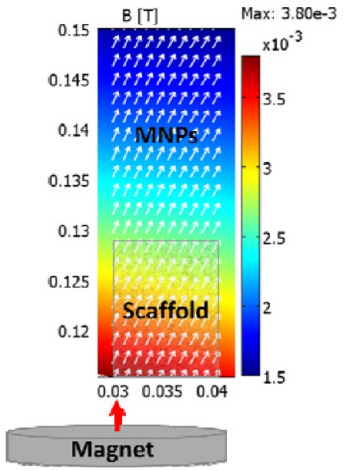

Figure 1. Distribution of magnetic field intensity (color bar) and its direction (arrows); the distances to magnet (left bar) are given in meters. The relative position of the magnet axis and the orientation of its magnetization are indicated by the red arrow.

DOI: 10.1021/acsami.5b00529
ACS Appl. Mater. Interfaces 2015, 7, 6282−6292

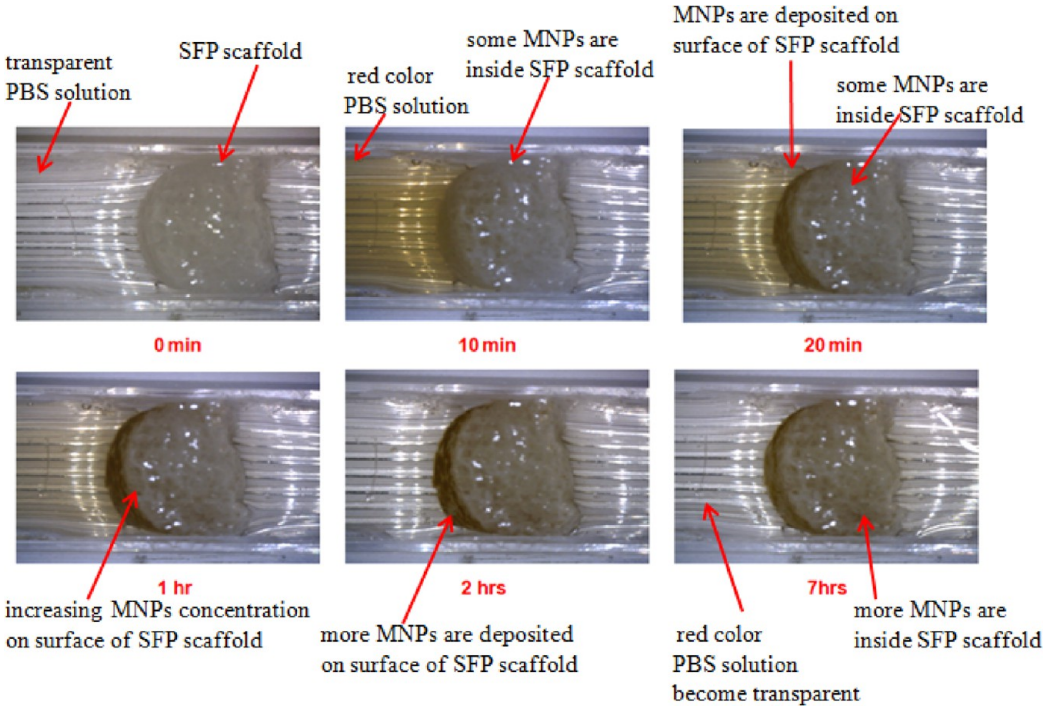

Figure 2. Diffusion of magnetic nanoparticles (MNPs) into silk fibroin protein (SFP) scaffolds at different time points (0 min, 10 min, 20 min, 1 h, 2 h, and 7 h) in phosphate buffer saline (PBS) medium under applied magnetic field. The MNPs accumulation within silk scaffold increases with increasing time.

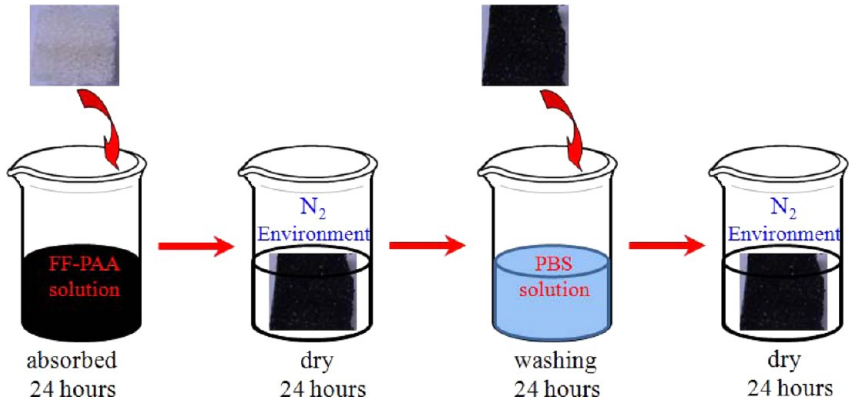

Figure 3. Schematic representation of magnetized silk scaffold by Ferrofluids poly-DL-aspartic acid (FF-PAA).

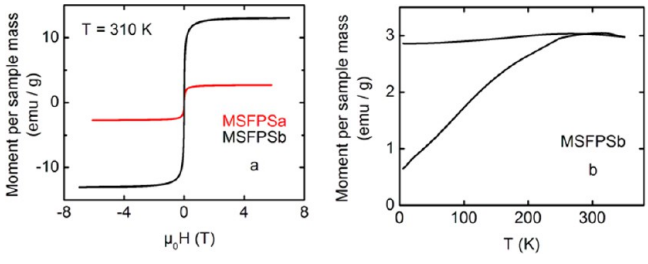

Figure 4. (a) Hysteresis loops at T = 310 K for magnetic silk scaffolds with two different magnetizations (MSFPSa and MSFPSb); (b) temperature sweeps for sample MSFPSb. Lower leg, field-heating at 0.01 T after previous zero-field cooling; upper leg, field-cooling at 0.01 T.

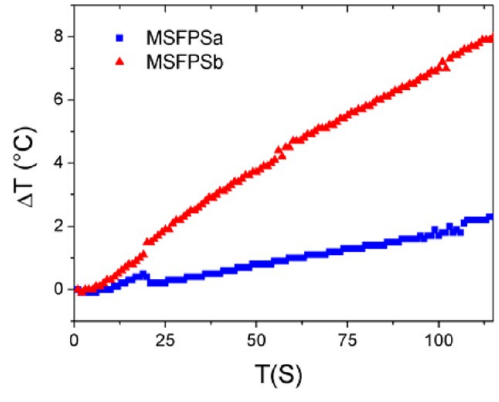

Figure 5. Magnetic silk scaffolds MSFPSa and MSFPSb with different hyperthermia properties.

sheet formation, which improved cell attachment and proliferation.[55,61] In the present study, we have used granular NaCl (particle size, 850−1000 μm) to have porous scaffolds.

DOI: 10.1021/acsami.5b00529
ACS Appl. Mater. Interfaces 2015, 7, 6282−6292

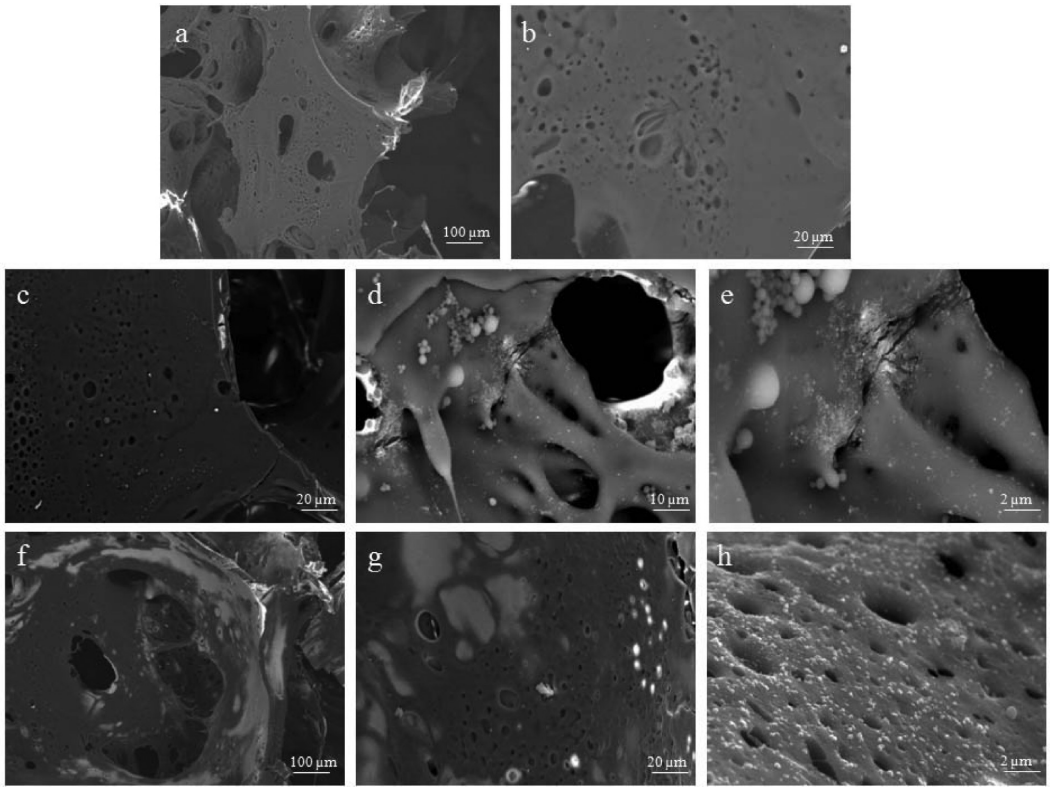

Figure 6. Morphologies of silk scaffold and magnetic silk scaffold were observed using a FE-SEM LEO 1530 (a,b) salt leaching SFPS, (c–e) low magnetized MSFPSa, and (f–h) high magnetized MSFPSb scaffolds, with an accelerating voltage of 18 kV.

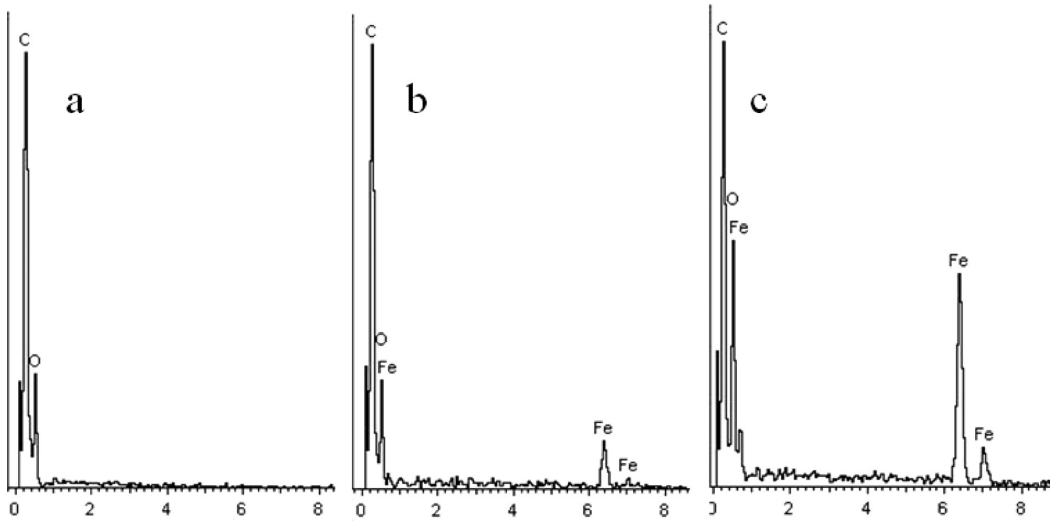

Figure 7. EDS spectra of silk scaffold and magnetic silk scaffold (MSFPSa and MSFPSb): (a) salt leaching SFP scaffolds, (b) low magnetized, and (c) high magnetized SFP scaffolds.

The NaCl particles' surface partially dissolves during the addition to silk solutions and generates scaffold size around 750 ± 20 μm with porosity 94 ± 0.2.[55,57,58]

3.2. Diffusion of MNPs into SFP Scaffolds. The diffusion of MNPs and conjugated MNPs with bioagents (growth factors, other proteins) in porous interconnected silk scaffolds can play a role in determining the overall potential of magnetic silk scaffolds in therapeutic applications. In the experiment, the MNPs diffusion into the SPF scaffold was induced by magnetic field: B = 2.1 ± 0.6 mT and B = 3.2 ± 0.5 mT in the MNPs and scaffold regions correspondingly. Figure 1 indicates the distribution of the magnetic field intensity (color bar) and its direction (arrows) in the above-mentioned regions.

The magnetic force acting on the MNPs is directly proportional to the magnetic field gradient that in our case was 0.055 ± 0.015 and 0.08 ± 0.02 T/m in the MNPs and scaffold regions correspondingly. These gradients were sufficient for moving MNPs into the scaffold. The diffusion increased and MNPs into silk scaffold leads to the accumulation of nanoparticles. The results also indicated that with different time points the diffusion of MNPs accumulated in the silk scaffold. This accumulation may be due to the chelation of

DOI: 10.1021/acsami.5b00529
ACS Appl. Mater. Interfaces 2015, 7, 6282–6292

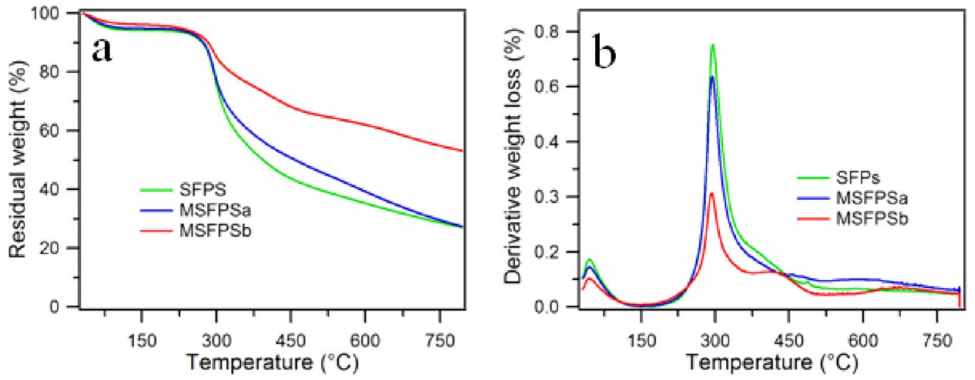

Figure 8. TGA spectra of SFP scaffold and magnetic silk: (a) residual weight loss and (b) derivative weight loss at 10 °C min^{-1} with a temperature range of 30−800 °C under 60 mL min^{-1} flow rate of nitrogen.

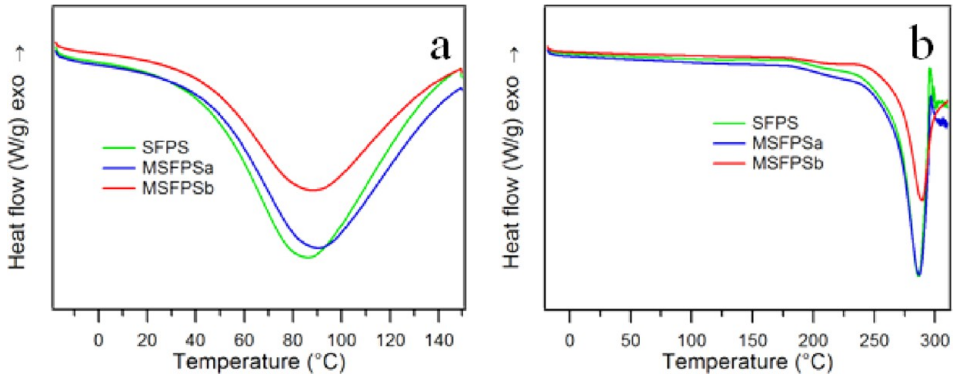

Figure 9. Differential scanning spectra of silk scaffolds and magnetic silk scaffolds: (a) first heating and (b) second heating spectra at a scan rate of 10 °C min^{-1} under a nitrogen atmosphere at 80 mL min^{-1} flow rate.

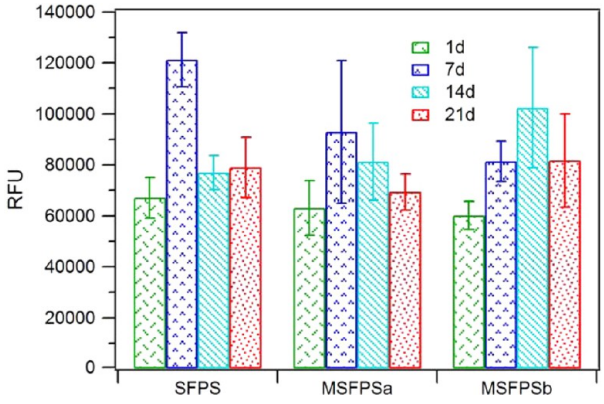

Figure 10. Viable cells cultured on silk (SFPS, control) and magnetized silk scaffolds SFPSa and SFPSb for 21 days. The amount of viable cells was quantified with the Prestoblue assay and represented as relative fluorescence units (RFU).

MNPs by the functional groups of SFPs (−COOH, $-NH_2$, and −OH) as well as physical entrapment. At 0 min the silk scaffold appeared white in color, while at 10 min the MNPs slowly start to deposit on the surface of the scaffolds and some MNPs accumulated in the scaffolds (Figure 2).

The accumulation of MNPs was evident at 20 min and became more pronounced at 1 and 2 h. At 7 h the MNPs were no longer visible on the surface as the MNPs were absorbed into the porous structure of the silk scaffolds.

3.3. Magnetization of Silk Scaffolds. Porous silk scaffolds with dimension 5 × 5 mm^3 were slowly soaked with two different FF-PAA concentrations of 50 and 200 μL/mL (Figure 3).

The scaffolds containing magnetic nanoparticles were allowed to stand in a nitrogen environment for 24 h to allow the magnetic nanoparticles to absorb into the micro-/nanopores of the scaffold. The magnetic scaffolds did not suffer from structural damage during the process, maintaining porosity and shape. Moreover, the magnetic particles were not released upon constant shaking in simulated body fluids over a period of 24 h.

3.4. Magnetization Measurements. The magnetic properties of magnetic silk scaffolds were acquired by the magnetization $M(T,B)$ of magnetic NPs, which are homogeneously dispersed inside the scaffolds. The narrow hysteresis loops of magnetic silk scaffolds are shown in Figure 4a. At T = 310 K, the magnetic silk scaffolds exhibited a ferromagnetic-like behavior with a saturation magnetization value of 2.7 and 13 emu/g, respectively, for samples MSFPSa and MSFPSb.

Almost full saturation is reached at low field, and is thus accessible by state-of-the-art implantable permanent magnets. These magnetization values are suitable for generating magnetic gradients. The coercive field of the magnetic silk scaffolds is negligible (approximately 15 Oe in both cases) and supports the expectation of a superparamagnetic character of the nanoparticles, which is determined by very weak magnetic interactions between the nanoparticles. Superparamagnetism is further confirmed by the temperature dependence of the magnetization of the silk samples recorded following a zero-field-cooling, field-heating, field-cooling protocol (Figure 4b): Heating the samples in a small field ($\mu_0 H$ = 0.01T) from an

DOI: 10.1021/acsami.5b00529
ACS Appl. Mater. Interfaces 2015, 7, 6282−6292

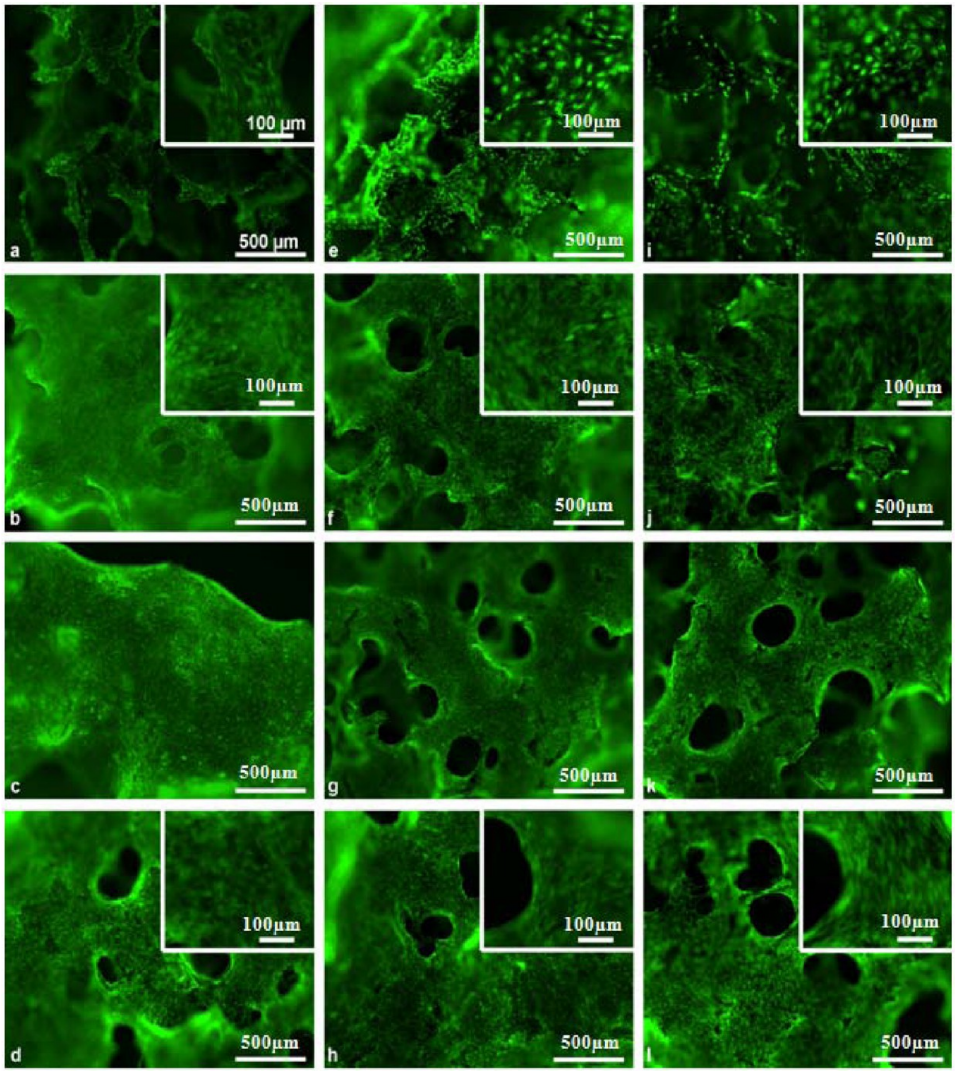

Figure 11. Cell viability and proliferation on control and magnetized silk scaffolds. Fluorescence microscopy (CaAM/PI staining) of MC3T3 cells cultured on the scaffolds for 1 day (a,e,i), 7 days (b,f,j), 14 days (c,g,k), and 21 days (d,h,l) for the SFPS control scaffolds (a−d) and magnetized scaffolds (MSFPSa (e−h) and MSFPSb (i−l)).

unpolarized state increases the magnetization due to thermal activation. Eventually, a crossover temperature is reached, above which the sample enters a paramagnetic regime with decreasing magnetization upon increase of temperature. Subsequent cooling in field confirms a fully polarized magnetic state below the crossover temperature. The slight decrease of magnetization in the field-cooling leg of the curve is most likely due to a tiny displacement of the sample in the course of the measuring process. Superparamagnetism of the MNPs is a necessary premise for the applicability of the scaffolds in the fields of biomedical engineering and bioengineering.

The magnetic behavior of superparamagnetic particles can be described by Langevin theory with the assumption that they are monodisperse, freely rotatable, and noninteracting particles.[64] The average particle size D can be determined by using the low-field expansion of Langevin's function, together with the zero-field susceptibility and the high-field saturation magnetization at fixed temperature.[65] For sample MSFPSa, we find D_m = 35 nm, and for MSFPSb, D = 23 nm. These effective magnetic D_m values are smaller than the nominal diameter of 50 nm. A possible explanation for effective magnetic diameters D_m being smaller than the nominal microscopically determined diameter is given in the MNP surface-layer atoms being strongly affected by the adsorbed molecules, the highly polar nature of which might lead to the formation of a thin surface layer of a nonmagnetic compound. Thus, only the inner cores of the MNPs might be magnetic. With D_m = 35 nm (for sample MSFPSa) as the average MNP diameter, ρ = 5.18 g/cm^3 as the density of the magnetite particles, together with an Fe_3O_4 bulk magnetization of 4 Bohr magnetons per formula unit, leads to an average particle's magnetic moment of 1.2 × 10^6 μ_B.

3.5. Magnetic-Hyperthermia Measurements. When MNPs are directly injected in an aqueous solution at the tumor site, there are difficulties to ensure that the particles remain at the targeted site.[66] Magnetic scaffold nanocomposites have the ability to encapsulate MNPs in a polymer matrix and deliver MNPs directly to tumor sites so that hyperthermia treatment is local. These magnetic scaffolds are able to be remotely heated upon exposure to an external alternating magnetic field. The heating mechanism for superparamagnetic particles is based on Brownian relaxation (rotation of the particle as a whole according to external magnetic field) and Néel effect (reorientation of the magnetization vector inside the magnetic core against an energy barrier).[67] Along with

DOI: 10.1021/acsami.5b00529
ACS Appl. Mater. Interfaces 2015, 7, 6282−6292

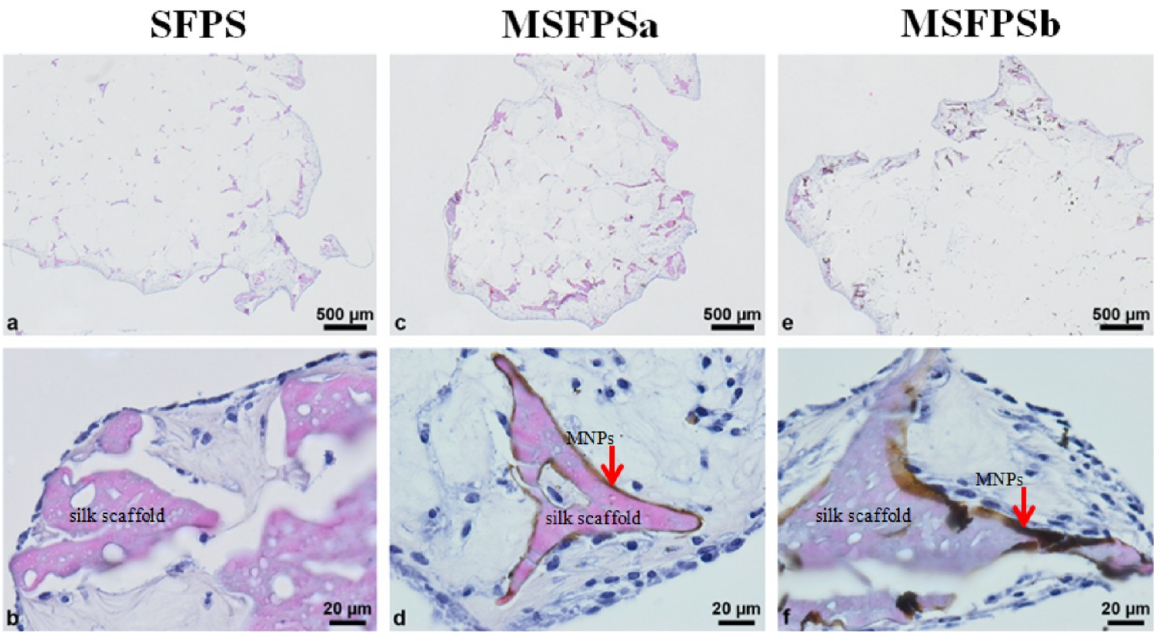

Figure 12. Colonization of MC3T3 cells on silk scaffold (control) and magnetized silk scaffolds. Histological analysis (H&E staining) of MC3T3 cells cultured on 3D scaffolds for 14 days. SFPS (control) (a,b), magnetized MSFPSa (c,d), and MSFPSb (e,f).

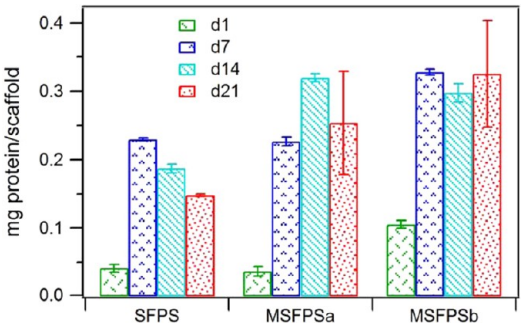

Figure 13. Protein content of silk and magnetized silk scaffolds cultured for 1, 7, 14, and 21 days in osteogenic medium (mean and SD, $n = 3$) with statistical significance ($P < 0.05$).

delivering heat, these systems would have the ability to deliver other therapeutic agents (chemotherapeutics, radionuclides, immunotherapeutics) outlined previously for a multimodality treatment. A handful of systems have already shown potential for this process. Such magnetically responsive materials offer the benefit of controlling drug release in either a single or a multiple pulse formulation, which benefits the patient by reducing the total amount of drug required to reach the effective dose, reducing the frequency of administration.

The magnetic silk scaffolds have a low saturation magnetization; however, they show excellent hyperthermia properties under exposure to an alternating magnetic field (Figure 5). This observation is promising for biomedical research, as well as for triggered release of drugs, growth factors, or other biomolecules.[52,68]

3.6. Scaffold Morphology by Field Emission Scanning Electron Microscopy (FE-SEM) and Composition by Energy Dispersive X-ray Spectrometry (EDS). The morphologies of the magnetized scaffolds were not substantially altered by the magnetization process (Figure 6), which indicates that the morphology of magnetized scaffolds was not affected by the loading of the MNPs.

Pore sizes did not differ significantly between the magnetized and the nonmagnetic silk scaffolds. MNPs appeared to be embedded within the scaffold walls, and no aggregation or clumps at 10 K were observed (Figure 6e and h). Very few MNPs clusters of 50−200 nm sizes were visible as white spots in the FE-SEM micrographs, which are representative of inorganic phases as well as iron oxide.

The results indicate that the silk has good interaction with MNPs, forming a homogeneous nanocomposite biomaterial with little aggregation of MNPs. The EDS spectra confirmed the presence of iron in magnetized scaffolds (Figure 7).

3.7. Thermogravimetric Analysis (TGA). The thermal stability of the MNPs encapsulated in silk scaffolds was analyzed by TGA. The TGA and derivative TGA curves are shown in Figure 8a and b. The TGA traces show a continuous weight loss up to 700 °C. The first step loss in the range of 30−120 °C was attributed to the loss of moisture or absorbed water; the results of TGA and derivative curve indicate that MSFPSb has less absorbed water as compared to MSFPSa and native silk scaffolds. This may be due to the presence of the nanostructured MNPs, which help in the faster evaporation of water. The second step is the continuous weight loss from 250 °C on due to the silk network decomposition at elevated temperatures. The derivative TGA curves showed that the maximum decomposition rate of the scaffolds occurred at 295 °C. In silk scaffolds, rapid weight loss was observed after 200 °C; there was a shoulder at ∼350−450 °C in the derivative TGA curve, which could be ascribed to oxidative decomposition of organic skeleton or C−C backbone of silk. However, scaffolds containing MNPs have different thermal degradation profiles from 300 to 700 °C even at low concentrations of MNPs, which might be due to the adhesive force between MNPs and the silk. The magnetized silk scaffold degradation process is MNP concentration dependent. In the case of MSFPSb derivative TGA curves, a small peak at ∼425 °C was evident, and the reason could be due to the phase transition of Fe_3O_4 to FeO or the decomposition of polymeric chain, which produces reducing gas that further reacts with

DOI: 10.1021/acsami.5b00529
ACS Appl. Mater. Interfaces 2015, 7, 6282−6292

Fe_3O_4.[69−73] The thermal investigation by TGA led to the observation that magnetized scaffolds possessed higher residue content at 700 °C due to the presence of magnetic nanoparticles as compared to nonmagnetized silk scaffolds.

3.8. Differential Scanning Calorimetry (DSC). The first heating (Figure 9a) curve shows MNPs infusion properties of the scaffolds as compared to pure silk scaffold, based on the result that the presence of the nanostructured MNPs resulted in faster evaporation of water evident from the shift in the spectra, which is in accordance with the TGA results. The second heating (Figure 9b) revealed a change in melting temperature prior to degradation, possibly due to the presence of the MNPs, which increased the thermal stability of the nanocomposite silk matrix.

3.9. Cell Culture. *3.9.1. Cell Viability, Adhesion, and Proliferation.* The amount of attached viable cells on the silk scaffolds and magnetic silk scaffolds was determined by PrestoBlue assay (Figure 10). Cells remained viable for a culture period of 21 days both in low and in high magnetic concentration scaffolds, comparable with the control silk scaffold.

The cells on the scaffolds were examined by fluorescence microscopy after live/dead staining (Figure 11). After 1 day cells were spread and showed a polygonal morphology, irrespective of the scaffold type (Figure 11a,e,i). From 7 days (Figure 11b,f,j), the blank and magnetized scaffolds were fully covered with a layer of viable cells. The cells remained viable after 14 (Figure 11c,g,k) and 21 days (Figure 11d,h,l).

3.9.2. Cellular Colonization of the Scaffolds. Cross sections of paraffin-embedded cell/scaffold constructs after 14 days in culture are presented in Figure 12. The silk and magnetized silk scaffolds were colonized at the edge of the scaffold (Figure 10a,c,e).

The cells followed the contours of the scaffolds (Figure 12b,d,f). A dark line (brown) of the magnetic nanoparticles was visible in the magnetic scaffolds (Figure 12d,f).

To evaluate tissue formation, the protein content was evaluated at specific time points (Figure 13). The cells, irrespective of scaffold type, proliferated starting from day 1 and reached a peak at 21 days. From the results, the total protein content of magnetized silk scaffolds was higher than that for the control silk scaffolds.

4. CONCLUSIONS

The feasibility of producing homogeneously magnetized porous magnetic silk scaffolds was confirmed by FE-SEM and EDS. Magnetic measurements revealed that scaffold magnetization can be described via superparamagnetic behavior, the latter representing a regime that can be considered appropriate for biomedical applications. Despite relatively low saturation magnetization, the scaffolds showed excellent hyperthermia properties under exposure to an alternating magnetic field. These promising results indicate the possible utilization of such scaffolds for the triggered release of drugs, growth factors, or other biomolecules. The magnetized silk scaffolds were nontoxic, and the presence of MNPs improved cell adhesion and colonization of osteogenic cells, indicating the suitability of such scaffolds for tissue engineering.

AUTHOR INFORMATION

Corresponding Authors

*Tel.: (617) 627-0851. Fax: (617) 627-3231. E-mail: david.kaplan@tufts.edu.

*E-mail: v.dediu@bo.ismn.cnr.it.

Present Address

◆Department of Applied Physics, Faculty of Physics, University of Santiago de Compostela, 15782 Santiago de Compostela, Spain.

Notes

The authors declare no competing financial interest.

ACKNOWLEDGMENTS

We would like to thank the EC-FP7 project MAGISTER (NMP3-LA-2008-214685), the NIH (EB002520), and the AFOSR for financial support. The support of the HLD at HZDR, member of the European Magnetic Field Laboratory (EMFL), is also acknowledged.

REFERENCES

(1) Zhang, W.; Wang, X.; Wang, S.; Zhao, J.; Xu, L.; Zhu, C.; Zeng, D.; Chen, J.; Zhang, Z.; Kaplan, D. L.; Jiang, X. The Use of Injectable Sonication-Induced Silk Hydrogel for Vegf165 and Bmp-2 Delivery for Elevation of the Maxillary Sinus Floor. *Biomaterials* **2011**, *32*, 9415−9424.

(2) Richardson, T. P.; Peters, M. C.; Ennett, A. B.; Mooney, D. J. Polymeric System for Dual Growth Factor Delivery. *Nat. Biotechnol.* **2001**, *19*, 1029−1034.

(3) Tessmar, J. K.; Göpferich, A. M. Matrices and Scaffolds for Protein Delivery in Tissue Engineering. *Adv. Drug Delivery Rev.* **2007**, *59*, 274−291.

(4) Chen, F.-M.; Zhang, M.; Wu, Z.-F. Toward Delivery of Multiple Growth Factors in Tissue Engineering. *Biomaterials* **2010**, *31*, 6279−6308.

(5) Lee, K.; Silva, E. A.; Mooney, D. J. Growth Factor Delivery-Based Tissue Engineering: General Approaches and a Review of Recent Developments. *J. R. Soc., Interface* **2011**, *8*, 153−170.

(6) Panigrahy, D.; Kalish, B. T.; Huang, S.; Bielenberg, D. R.; Le, H. D.; Yang, J.; Edin, M. L.; Lee, C. R.; Benny, O.; Mudge, D. K.; Butterfield, C. E.; Mammoto, A.; Mammoto, T.; Inceoglu, B.; Jenkins, R. L.; Simpson, M. A.; Akino, T.; Lih, F. B.; Tomer, K. B.; Ingber, D. E.; Hammock, B. D.; Falck, J. R.; Manthati, V. L.; Kaipainen, A.; D'Amore, P. A.; Puder, M.; Zeldin, D. C.; Kieran, M. W. Epoxyeicosanoids Promote Organ and Tissue Regeneration. *Proc. Natl. Acad. Sci. U.S.A.* **2013**, *110*, 13528−13533.

(7) Gil, S.; Mano, J. F. Magnetic Composite Biomaterials for Tissue Engineering. *Biomater. Sci.* **2014**, *2*, 812−818.

(8) Santo, V. E.; Rodrigues, M. T.; Gomes, M. E. Contributions and Future Perspectives on the Use of Magnetic Nanoparticles as Diagnostic and Therapeutic Tools in the Field of Regenerative Medicine. *Expert Rev. Mol. Diagn.* **2013**, *13*, 553−566.

(9) Xu, H.-Y.; Gu, N. Magnetic Responsive Scaffolds and Magnetic Fields in Bone Repair and Regeneration. *Front. Mater. Sci.* **2014**, *8*, 20−31.

(10) Skaat, H.; Ziv-Polat, O.; Shahar, A.; Last, D.; Mardor, Y.; Margel, S. Magnetic Scaffolds Enriched with Bioactive Nanoparticles for Tissue Engineering. *Adv. Healthcare Mater.* **2012**, *1*, 168−171.

(11) Singh, R. K.; Patel, K. D.; Lee, J. H.; Lee, E.-J.; Kim, J.-H.; Kim, T.-H.; Kim, H.-W. Potential of Magnetic Nanofiber Scaffolds with Mechanical and Biological Properties Applicable for Bone Regeneration. *PLoS One* **2014**, *9*, e91584.

(12) Altman, G. H.; Diaz, F.; Jakuba, C.; Calabro, T.; Horan, R. L.; Chen, J.; Lu, H.; Richmond, J.; Kaplan, D. L. Silk-Based Biomaterials. *Biomaterials* **2003**, *24*, 401−416.

(13) Wang, Y.; Kim, H.-J.; Vunjak-Novakovic, G.; Kaplan, D. L. Stem Cell-Based Tissue Engineering with Silk Biomaterials. *Biomaterials* **2006**, *27*, 6064−6082.

(14) Dobb, M. G.; Fraser, R. D. B.; Macrae, T. P. The Fine Structure of Silk Fibroin. *J. Cell Biol.* **1967**, *32*, 289−295.

DOI: 10.1021/acsami.5b00529
ACS Appl. Mater. Interfaces 2015, 7, 6282−6292

(15) Murphy, A. R.; Kaplan, D. L. Biomedical Applications of Chemically-Modified Silk Fibroin. *J. Mater. Chem.* **2009**, *19*, 6443−6450.
(16) Guziewicz, N.; Best, A.; Perez-Ramirez, B.; Kaplan, D. L. Lyophilized Silk Fibroin Hydrogels for the Sustained Local Delivery of Therapeutic Monoclonal Antibodies. *Biomaterials* **2011**, *32*, 2642−2650.
(17) Kantipuly, C.; Katragadda, S.; Chow, A.; Gesser, H. D. Chelating Polymers and Related Supports for Separation and Preconcentration of Trace Metals. *Talanta* **1990**, *37*, 491−517.
(18) Kawamura, Y.; Mitsuhashi, M.; Tanibe, H.; Yoshida, H. Adsorption of Metal Ions on Polyaminated Highly Porous Chitosan Chelating Resin. *Ind. Eng. Chem. Res.* **1993**, *32*, 386−391.
(19) Wan Ngah, W. S.; Teong, L. C.; Hanafiah, M. A. K. M. Adsorption of Dyes and Heavy Metal Ions by Chitosan Composites: A Review. *Carbohydr. Polym.* **2011**, *83*, 1446−1456.
(20) Carrell, H. L.; Glusker, J. P.; Piercy, E. A.; Stallings, W. C.; Zacharias, D. E.; Davis, R. L.; Astbury, C.; Kennard, C. H. L. Metal Chelation Versus Internal Hydrogen Bonding of The.Alpha.-Hydroxy Carboxylate Group. *J. Am. Chem. Soc.* **1987**, *109*, 8067−8071.
(21) Mouriño, V.; Cattalini, J. P.; Boccaccini, A. R. Metallic Ions as Therapeutic Agents in Tissue Engineering Scaffolds: An Overview of Their Biological Applications and Strategies for New Developments. *J. R. Soc., Interface* **2011**.
(22) Yokoyama, M. Clinical Applications of Polymeric Micelle Carrier Systems in Chemotherapy and Image Diagnosis of Solid Tumors. *J. Exp. Clin. Med.* **2011**, *3*, 151−158.
(23) De León-Rodríguez, L. M.; Kovacs, Z. The Synthesis and Chelation Chemistry of Dota−Peptide Conjugates. *Bioconjugate Chem.* **2007**, *19*, 391−402.
(24) Bock, N.; Riminucci, A.; Dionigi, C.; Russo, A.; Tampieri, A.; Landi, E.; Goranov, V. A.; Marcacci, M.; Dediu, V. A Novel Route in Bone Tissue Engineering: Magnetic Biomimetic Scaffolds. *Acta Biomater.* **2010**, *6*, 786−796.
(25) Panseri, S.; Russo, A.; Sartori, M.; Giavaresi, G.; Sandri, M.; Fini, M.; Maltarello, M. C.; Shelyakova, T.; Ortolani, A.; Visani, A.; Dediu, V.; Tampieri, A.; Marcacci, M. Modifying Bone Scaffold Architecture in Vivo with Permanent Magnets to Facilitate Fixation of Magnetic Scaffolds. *Bone* **2013**, *56*, 432−439.
(26) Kim, J.; Chung, S. E.; Choi, S. E.; Lee, H.; Kim, J.; Kwon, S. Programming Magnetic Anisotropy in Polymeric Microactuators. *Nat. Mater.* **2011**, *10*, 747−752.
(27) Panseri, S.; Cunha, C.; D'Alessandro, T.; Sandri, M.; Russo, A.; Giavaresi, G.; Marcacci, M.; Hung, C. T.; Tampieri, A. Magnetic Hydroxyapatite Bone Substitutes to Enhance Tissue Regeneration: Evaluation in Vitro Using Osteoblast-Like Cells and in Vivo in a Bone Defect. *PLoS One* **2012**, *7*, e38710.
(28) Li, L.; Jiang, W.; Luo, K.; Song, H. M.; Lan, F.; Wu, Y.; Gu, Z. W. Superparamagnetic Iron Oxide Nanoparticles as Mri Contrast Agents for Non-Invasive Stem Cell Labeling and Tracking. *Theranostics* **2013**, *3*, 595−615.
(29) Li, B.; Jia, D.; Zhou, Y.; Hu, Q.; Cai, W. In Situ Hybridization to Chitosan/Magnetite Nanocomposite Induced by the Magnetic Field. *J. Magn. Magn. Mater.* **2006**, *306*, 223−227.
(30) Li, Y.; Huang, G.; Zhang, X.; Li, B.; Chen, Y.; Lu, T.; Lu, T. J.; Xu, F. Magnetic Hydrogels and Their Potential Biomedical Applications. *Adv. Funct. Mater.* **2013**, *23*, 660−672.
(31) Huang, D.-M.; Hsiao, J.-K.; Chen, Y.-C.; Chien, L.-Y.; Yao, M.; Chen, Y.-K.; Ko, B.-S.; Hsu, S.-C.; Tai, L.-A.; Cheng, H.-Y.; Wang, S.-W.; Yang, C.-S.; Chen, Y.-C. The Promotion of Human Mesenchymal Stem Cell Proliferation by Superparamagnetic Iron Oxide Nanoparticles. *Biomaterials* **2009**, *30*, 3645−3651.
(32) Hou, R.; Zhang, G.; Du, G.; Zhan, D.; Cong, Y.; Cheng, Y.; Fu, J. Magnetic Nanohydroxyapatite/Pva Composite Hydrogels for Promoted Osteoblast Adhesion and Proliferation. *Colloids Surf., B* **2013**, *103*, 318−325.
(33) Kim, J.-J.; Singh, R. K.; Seo, S.-J.; Kim, T.-H.; Kim, J.-H.; Lee, E.-J.; Kim, H.-W. Magnetic Scaffolds of Polycaprolactone with Functionalized Magnetite Nanoparticles: Physicochemical, Mechanical, and Biological Properties Effective for Bone Regeneration. *RSC Adv.* **2014**, *4*, 17325−17336.
(34) Dashnyam, K.; Perez, R. A.; Singh, R. K.; Lee, E.-J.; Kim, H.-W. Hybrid Magnetic Scaffolds of Gelatin-Siloxane Incorporated with Magnetite Nanoparticles Effective for Bone Tissue Engineering. *RSC Adv.* **2014**, *4*, 40841−40851.
(35) Tampieri, A.; Iafisco, M.; Sandri, M.; Panseri, S.; Cunha, C.; Sprio, S.; Savini, E.; Uhlarz, M.; Herrmannsdörfer, T. Magnetic Bioinspired Hybrid Nanostructured Collagen−Hydroxyapatite Scaffolds Supporting Cell Proliferation and Tuning Regenerative Process. *ACS Appl. Mater. Interfaces* **2014**, *6*, 15697−15707.
(36) Sapir, Y.; Cohen, S.; Friedman, G.; Polyak, B. The Promotion of In vitro Vessel-Like Organization of Endothelial Cells in Magnetically Responsive Alginate Scaffolds. *Biomaterials* **2012**, *33*, 4100−4109.
(37) Thevenot, J.; Oliveira, H.; Sandre, O.; Lecommandoux, S. Magnetic Responsive Polymer Composite Materials. *Chem. Soc. Rev.* **2013**, *42*, 7099−7116.
(38) Ilg, P. Stimuli-Responsive Hydrogels Cross-Linked by Magnetic Nanoparticles. *Soft Matter* **2013**, *9*, 3465−3468.
(39) Yiu, H. H. P.; Liu, K.-K. Mechanical and Magnetic Stimulation on Cells for Bone Regeneration. *Biomechanics of Hard Tissues*; Wiley-VCH Verlag GmbH & Co. KGaA: New York, 2010; pp 193−207.
(40) Stock, M.; Kirchner, B.; Waibler, D.; Cowley, D. E.; Pfaffl, M. W.; Kuehn, R. Effect of Magnetic Stimulation on the Gene Expression Profile of in Vitro Cultured Neural Cells. *Neurosci. Lett.* **2012**, *526*, 122−127.
(41) Pashut, T.; Wolfus, S.; Friedman, A.; Lavidor, M.; Bar-Gad, I.; Yeshurun, Y.; Korngreen, A. Mechanisms of Magnetic Stimulation of Central Nervous System Neurons. *PLoS Comput. Biol.* **2011**, *7*, e1002022.
(42) Hellmann, J.; Jüttner, R.; Roth, C.; Bajbouj, M.; Kirste, I.; Heuser, I.; Gertz, K.; Endres, M.; Kronenberg, G. Repetitive Magnetic Stimulation of Human-Derived Neuron-Like Cells Activates Camp-Creb Pathway. *Eur. Arch. Psychiatry Clin. Neurosci.* **2012**, *262*, 87−91.
(43) Sensenig, R.; Sapir, Y.; MacDonald, C.; Cohen, S.; Polyak, B. Magnetic Nanoparticle-Based Approaches to Locally Target Therapy and Enhance Tissue Regeneration in Vivo. *Nanomedicine* **2012**, *7*, 1425−1442.
(44) Xiong, F.; Chen, Y.; Chen, J.; Yang, B.; Zhang, Y.; Gao, H.; Hua, Z.; Gu, N. Rubik-Like Magnetic Nanoassemblies as an Efficient Drug Multifunctional Carrier for Cancer Theranostics. *J. Controlled Release* **2013**, *172*, 993−1001.
(45) Wang, C.; Ravi, S.; Martinez, G. V.; Chinnasamy, V.; Raulji, P.; Howell, M.; Davis, Y.; Mallela, J.; Seehra, M. S.; Mohapatra, S. Dual-Purpose Magnetic Micelles for Mri and Gene Delivery. *J. Controlled Release* **2012**, *163*, 82−92.
(46) Colomb, J.; Louie, K.; Massia, S. P.; Bennett, K. M. Self-Degrading, Mri-Detectable Hydrogel Sensors with Picomolar Target Sensitivity. *Magn. Reson. Med.* **2010**, *64*, 1792−1799.
(47) Shin, M. K.; Kim, S. I.; Kim, S. J.; Park, S. Y.; Hyun, Y. H.; Lee, Y.; Lee, K. E.; Han, S.-S.; Jang, D.-P.; Kim, Y.-B.; Cho, Z.-H.; So, I.; Spinks, G. M. Controlled Magnetic Nanofiber Hydrogels by Clustering Ferritin. *Langmuir* **2008**, *24*, 12107−12111.
(48) Zhang, Y.; Sun, Y.; Yang, X.; Hilborn, J.; Heerschap, A.; Ossipov, D. A. Injectable in Situ Forming Hybrid Iron Oxide-Hyaluronic Acid Hydrogel for Magnetic Resonance Imaging and Drug Delivery. *Macromol. Biosci.* **2014**, *14*, 1249−1259.
(49) Lee, Y.-C.; Gajdosik, M.; Josic, D.; Lin, S.-H. Plasma Membrane Isolation Using Immobilized Concanavalin a Magnetic Beads. In *Liver Proteomics*; Josic, D., Hixson, D. C., Eds.; Humana Press: Totowa, NJ, 2012; Chapter 3, pp 29−41.
(50) Madaeni, S. S.; Enayati, E.; Vatanpour, V. Separation of Nitrogen and Oxygen Gases by Polymeric Membrane Embedded with Magnetic Nano-Particle. *Polym. Adv. Technol.* **2011**, *22*, 2556−2563.
(51) Meenach, S. A.; Hilt, J. Z.; Anderson, K. W. Poly(Ethylene Glycol)-Based Magnetic Hydrogel Nanocomposites for Hyperthermia Cancer Therapy. *Acta Biomater.* **2010**, *6*, 1039−1046.
(52) Lin, T.-C.; Lin, F.-H.; Lin, J.-C. In Vitro Feasibility Study of the Use of a Magnetic Electrospun Chitosan Nanofiber Composite for

DOI: 10.1021/acsami.5b00529
ACS Appl. Mater. Interfaces 2015, 7, 6282−6292

Hyperthermia Treatment of Tumor Cells. *Acta Biomater.* **2012**, *8*, 2704−2711.
(53) Samal, S. K.; Kaplan, D. L.; Chiellini, E. Ultrasound Sonication Effects on Silk Fibroin Protein. *Macromol. Mater. Eng.* **2013**, *298*, 1201−1208.
(54) Samal, S. K.; Dash, M.; Chiellini, F.; Kaplan, D. L.; Chiellini, E. Silk Microgels Formed by Proteolytic Enzyme Activity. *Acta Biomater.* **2013**, *9*, 8192−8199.
(55) Kim, U.-J.; Park, J.; Joo Kim, H.; Wada, M.; Kaplan, D. L. Three-Dimensional Aqueous-Derived Biomaterial Scaffolds from Silk Fibroin. *Biomaterials* **2005**, *26*, 2775−2785.
(56) Wang, Y.; Kim, U.-J.; Blasioli, D. J.; Kim, H.-J.; Kaplan, D. L. In Vitro Cartilage Tissue Engineering with 3d Porous Aqueous-Derived Silk Scaffolds and Mesenchymal Stem Cells. *Biomaterials* **2005**, *26*, 7082−7094.
(57) Kim, H. J.; Kim, U.-J.; Kim, H. S.; Li, C.; Wada, M.; Leisk, G. G.; Kaplan, D. L. Bone Tissue Engineering with Premineralized Silk Scaffolds. *Bone* **2008**, *42*, 1226−1234.
(58) Kaplan, D. L.; Kim, U.-J.; Park, J.; Jin, H.-J. Concentrated Aqueous Silk Fibroin Solution and Use Thereof. PCT/US2004/011199, 2005.
(59) Samal, S.; Fernandes, E.; Chiellini, F.; Chiellini, E. Thermal Analysis of Pva/Cnts 2d Membrane. *J. Therm. Anal. Calorim.* **2009**, *97*, 859−864.
(60) Rockwood, D. N.; Preda, R. C.; Yucel, T.; Wang, X. Q.; Lovett, M. L.; Kaplan, D. L. Materials Fabrication from Bombyx Mori Silk Fibroin. *Nat. Protoc.* **2011**, *6*, 1612−1631.
(61) Vepari, C.; Kaplan, D. L. Silk as a Biomaterial. *Prog. Polym. Sci.* **2007**, *32*, 991−1007.
(62) Nazarov, R.; Jin, H.-J.; Kaplan, D. L. Porous 3-D Scaffolds from Regenerated Silk Fibroin. *Biomacromolecules* **2004**, *5*, 718−726.
(63) Ak, F.; Oztoprak, Z.; Karakutuk, I.; Okay, O. Macroporous Silk Fibroin Cryogels. *Biomacromolecules* **2013**, *14*, 719−727.
(64) Coey, J. M. D. *Magnetism and Magnetic Materials*; Cambridge University Press: New York, 2010.
(65) Kim, D. K.; Zhang, Y.; Voit, W.; Rao, K. V.; Muhammed, M. Synthesis and Characterization of Surfactant-Coated Superparamagnetic Monodispersed Iron Oxide Nanoparticles. *J. Magn. Magn. Mater.* **2001**, *225*, 30−36.
(66) Chorny, M.; Fishbein, I.; Forbes, S.; Alferiev, I. Magnetic Nanoparticles for Targeted Vascular Delivery. *IUBMB Life* **2011**, *63*, 613−620.
(67) Babincová, M.; Leszczynska, D.; Sourivong, P.; Čičmanec, P.; Babinec, P. Superparamagnetic Gel as a Novel Material for Electromagnetically Induced Hyperthermia. *J. Magn. Magn. Mater.* **2001**, *225*, 109−112.
(68) Wu, C.; Fan, W.; Zhu, Y.; Gelinsky, M.; Chang, J.; Cuniberti, G.; Albrecht, V.; Friis, T.; Xiao, Y. Multifunctional Magnetic Mesoporous Bioactive Glass Scaffolds with a Hierarchical Pore Structure. *Acta Biomater.* **2011**, *7*, 3563−3572.
(69) Khoobi, M.; Delshad, T. M.; Vosooghi, M.; Alipour, M.; Hamadi, H.; Alipour, E.; Hamedani, M. P.; Sadat ebrahimi, S. E.; Safaei, Z.; Foroumadi, A.; Shafiee, A. Polyethyleneimine-Modified Superparamagnetic Fe_3O_4 Nanoparticles: An Efficient, Reusable and Water Tolerance Nanocatalyst. *J. Magn. Magn. Mater.* **2015**, *375*, 217−226.
(70) Rahman, O. u.; Mohapatra, S. C.; Ahmad, S. Fe_3O_4 Inverse Spinal Super Paramagnetic Nanoparticles. *Mater. Chem. Phys.* **2012**, *132*, 196−202.
(71) Sun, X.-F.; Jing, Z.; Wang, H.; Liu, Y. Physical−Chemical Properties of Xylan/Paac Magnetic Semi-Interpenetrating Network Hydrogel *Polym. Compos.* **2014**.
(72) Petcharoen, K.; Sirivat, A. Synthesis and Characterization of Magnetite Nanoparticles Via the Chemical Co-Precipitation Method. *Mater. Sci. Eng., B* **2012**, *177*, 421−427.
(73) Yang, K.; Peng, H.; Wen, Y.; Li, N. Re-Examination of Characteristic Ftir Spectrum of Secondary Layer in Bilayer Oleic Acid-Coated Fe_3O_4 Nanoparticles. *Appl. Surf. Sci.* **2010**, *256*, 3093−3097.

DOI: 10.1021/acsami.5b00529
ACS Appl. Mater. Interfaces 2015, 7, 6282−6292